GEOMETRY ASSOCIATED WITH THE COLLISION MANIFOLD

Joshua T. Fitzgerald[a,*], Aaron J. Rosengren[b], Shane D. Ross[a,b,c]

[a]Engineering Mechanics Program, Virginia Tech, Blacksburg, VA 24061, USA
[b]Mechanical and Aerospace Engineering, University of California, San Diego, CA, USA
[c]Aerospace and Ocean Engineering, Virginia Tech, Blacksburg, VA 24061, USA

Abstract

Neighborhoods of the Lagrange points control phase space transport at low energies in the circular restricted three-body problem because of the geometry of the forbidden region. At high energies, the forbidden region vanishes and the linearized dynamics about the Lagrange points no longer controls transit. "Arches of chaos" spanning solar system phase space were recently discovered which induce marked phase space stretching. We demonstrate numerically that the arches are the intersections of the stable and unstable manifolds to the singularities at the primaries with a specific surface of section. We explore how trajectories near these manifolds evolve and show how they connect to patched conics theory.

Keywords: Astrodynamics, Three-body problem, Levi-Civita regularization, Collision manifold, Arches of chaos

1. Introduction

The collinear Lagrange points anchor a fractal web of manifolds which transport particles throughout the Solar System. The phase space structure emanating from the Lagrange points was first analyzed within the circular restricted three-body problem, or CR3BP (Conley, 1968, 1969; McGehee, 1969; Llibre et al., 1985; Astakhov & Farrelly, 2004; Onozaki et al., 2017; Oshima et al., 2017; Topputo, 2013), but recent studies have investigated more general dynamical models, such as periodically perturbed problems (Jorba et al., 2020; McCarthy & Howell, 2020; Fitzgerald & Ross, 2022; Kumar et al., 2022; Oshima, 2022). The resultant theory of low energy transport is well-understood and has proven invaluable for both understanding the motions of natural celestial bodies (Koon et al., 2001; Jaffé et al., 2002) and planning spacecraft missions (Lo et al., 2001; Farquhar, 2001; Wu et al., 2012). Applications of the theory outside of astrodynamics span a wide range of topics, from chemical reaction dynamics (Bartsch et al., 2008) to snap-through buckling (Zhong et al., 2017; Zhong & Ross, 2021). However, for reasons that will be discussed in this study, low energy transport theory does not govern particle motion within sufficiently high energy regimes, and so different dynamical sets must take precedence.

Recent numerical investigations into solar system dynamics have revealed "arches of chaos" stretching throughout the phase space (Todorović et al., 2020). These objects induce dramatic rates of divergence between nearby trajectories on either side, suggesting that a mechanism of underlying phase space structures is responsible. The arch structure exists not only when all seven planets are considered but also when the dynamics are simplified to the Sun-Jupiter-particle system, suggesting that the core phenomenon arises in the restricted three-body problem. The current work will demonstrate that the stable and unstable manifolds to the CR3BP's singularities are responsible for the arches of chaos.

2. Introduction to the Arches of Chaos

2.1. The Fast Lyapunov Indicator

The Fast Lyapunov Indicator (FLI) is a computational method used to find chaotic regions and other phase space structures in a dynamical system (Froeschlé et al., 1997b,a).

Consider a manifold M where the n-dimensional tangent space at each $p \in M$ is T_pM. An autonomous dynamical system with time variable t on M induces a flow $\phi_t : M \to M$. Let $\left\{ \frac{\partial}{\partial x^1}\Big|_p, \ldots, \frac{\partial}{\partial x^n}\Big|_p \right\}$ be a basis for T_pM. Then the FLI at time t, with initial condition x_0 at $t = 0$, is $\psi_t : M \times \mathbb{R} \to \mathbb{R}^+$ such that

$$\psi(x_0, t) = \left(\sup_{i \in \{1,\ldots,n\}} \left\{ \left\| (\phi_{t,*})_{x_0} \frac{\partial}{\partial x^i}\Big|_{x_0} \right\| \right\} \right)^{-1}$$

*Corresponding author

Email addresses: joshfitz@vt.edu (Joshua T. Fitzgerald), ajrosengren@ucsd.edu (Aaron J. Rosengren), sdross@vt.edu (Shane D. Ross)

where $(\phi_{t,*})_{x_0}$ is the pushforward induced by ϕ_t at x_0 (Froeschlé et al., 1997b).

Because the FLI distinguishes regions of greater and lesser local "stretching", calculating it for grids of initial conditions facilitates detecting chaos-inducing structures. However, the Fast Lyapunov Indicator detects chaotic sets but does not indicate what dynamics *created* them. Additional methods are needed, and so explaining the dynamical geometry underlying the arches of chaos is the primary aim of this study.

2.2. The Arches of Chaos

A recent paper by Todorović et al. describes regions of high local stretching discovered by computing the FLI for selected initial conditions in solar system models (2020). One model incorporates the seven major planets, whereas the other is simpler and only incorporates the Sun and Jupiter. Calculating the FLI over dense grids of initial conditions in both models gradually reveals, over sufficient timescales, the arch-like regions seen in Figure 1. Much of this picture persists regardless of the model employed, which led the authors to conclude that interactions with Jupiter dominate the dynamics (Todorović et al., 2020).

The manifold structures associated with the arches of chaos appear and operate over fast timescales: several decades rather than tens of thousands of years. In this regard, they operate much faster than the timescales typically used in solar system dynamics (Todorović et al., 2020). Because of their higher energies and faster transit times, they also differ from the low-energy manifolds, which can require thousands of years to successfully transfer particles between planets (Werner, 2022). As shown in Figure 1, the stable manifolds to the collinear Lagrange points bound the arches when depicted in *a*-*e* space.

2.2.1. The surface of initial conditions

The arches of chaos are computed using initial conditions lying on a surface of constant mean anomaly M, inclination, argument of perihelion ω, and longitude of the ascending node Ω which is parameterized by the semi-major axis a and eccentricity e of the initial conditions. For initial epoch 30 September 2012, i, ω, and Ω for all initial conditions are set to the inclination, argument of perihelion, and longitude of the ascending node of Jupiter's orbit, and M for all initial conditions is set 60° ahead of the mean anomaly of Jupiter's orbit. These values correspond to trajectories whose position space projections begin evolution near the Sun-Jupiter L_4 Lagrange point (Todorović et al., 2020).

3. The regularization of the circular restricted three-body problem

3.1. The CR3BP

The circular restricted three-body problem concerns the motion of a particle P subject to the gravitational influence of two masses $m_1 > m_2$, which both circle their common barycenter O. For the remainder of this paper, we restrict analysis to the planar CR3BP (PCR3BP), in which P is constrained to the plane of motion of m_1 and m_2. The generalization to the spatial case is straightforward.

We write the equations of motion within a rotating reference frame whose origin is O and whose x-axis and y-axis point along the line between m_1 and m_2 and along the direction of motion of m_2, respectively (see Figure 2).

The equations of motion in the PCR3BP are Hamilton's canonical equations generated by the following Hamiltonian (Koon et al., 2022):

$$H_{\mathrm{CR3BP}} = \frac{1}{2}\left(p_x^2 + p_y^2\right) - xp_y + yp_x - \frac{1-\mu}{r_1} - \frac{\mu}{r_2} \tag{1}$$

where

$$r_1 = \sqrt{(x+\mu)^2 + y^2}, \quad r_2 = \sqrt{(x-1+\mu)^2 + y^2}$$

and $\mu = m_2/(m_1 + m_2)$ is the mass parameter.

3.2. The irrelevance of the Lagrange points

At low energies, phase space transport in the PCR3BP is controlled by the equilibria of the equations of motion, which are called the Lagrange points (Conley, 1968, 1969; McGehee, 1969; Koon et al., 2022). In the time-perturbed PCR3BP, phase space transport at low energies is controlled by generalizations of the Lagrange points sometimes called *dynamical replacements to the Lagrange points* or *Lagrange manifolds* (Jorba et al., 2020; Fitzgerald & Ross, 2022).

At high energies, the Lagrange points or Lagrange manifolds no longer control phase space transport. To understand why, vary the Hamiltonian energy and consider the evolution of the *forbidden realm*. Fix $H_{\mathrm{CR3BP}} = E \in \mathbb{R}$ to be the (conserved) energy of a trajectory. P can only move throughout the *Hill's region*, the subset of position space accessible for the chosen E. The inaccessible remainder is called the *forbidden realm*. The forbidden realm may exhibit one of five qualitatively distinct geometries corresponding to different intervals of E (see Figure 3):

1. For $E < E_1$, P is confined to neighborhoods around m_1 or m_2 or to an area exterior to the forbidden realm.
2. For $E_1 < E < E_2$, P is confined to neighborhoods around m_1 or m_2 or to an area exterior to the forbidden realm.

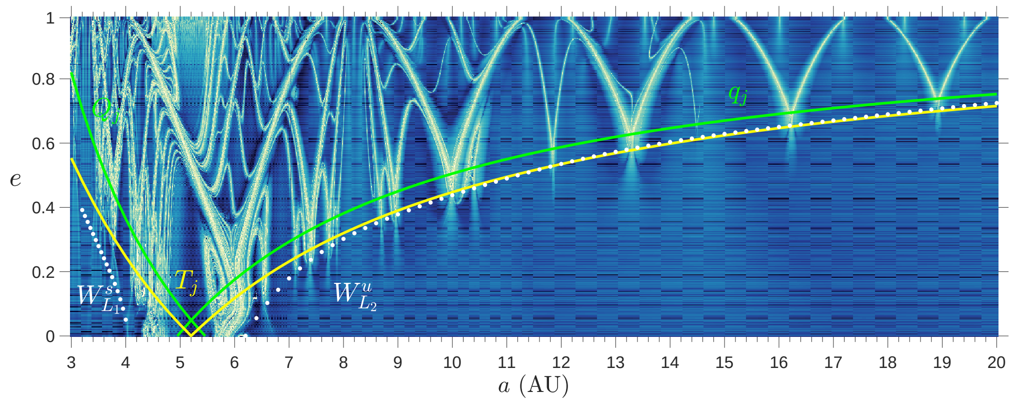

Figure 1: FLI maps of a grid of initial conditions with varying semi-major axes a and eccentricities e reveal a complex series of arch-like structures, the Arches of Chaos, in the Sun-Jupiter restricted three-body problem. Regions with lighter colors correspond to higher values of the FLI and therefore to higher trajectory divergence, which suggests the presence of stable and unstable manifolds. q_j and Q_j are Jupiter's perihelion and aphelion lines, respectively, and $T_j = 3$ is a Jupiter Tisserand curve. $W^S_{L_1}$ and $W^S_{L_2}$ are the stable manifold curves of the Sun-Jupiter L_1 and L_2 points, respectively. Figure edited from Todorović et al. (2020).

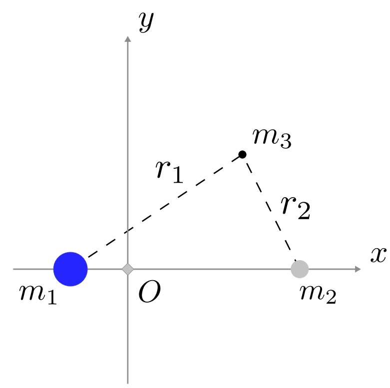

Figure 2: A schematic of the planar circular restricted three-body problem viewed in the rotating frame.

3. For $E_2 < E < E_3$, P gains the ability to travel between the m_1 and m_2 neighborhoods.
4. For $E_3 < E < E_4$, P gains the ability to travel between the m_2 neighborhood and the exterior area.
5. For $E_5 < E$, the forbidden realm is no longer present.

The dynamics of low-energy transport rely on the existence of the "neck regions" linking the neighborhoods. In the Case 3 energy interval often used in trajectory design, P can access all three regions of interest but is forced to travel through the necks. The neck regions correspond to the neighborhoods of the Lagrange points, which is why the linearized geometry about the Lagrange points is responsible for governing transit at low energies.

At high energies such as those within the Case 5 energy interval, the forbidden region disappears and so the neck regions no longer link regions of position space. The Lagrange points are no longer key to phase space transport.

3.3. Introduction to the Levi-Civita regularization

We will show in the remainder of the paper that the locations of m_1 and m_2 dictate high-energy transport, but we

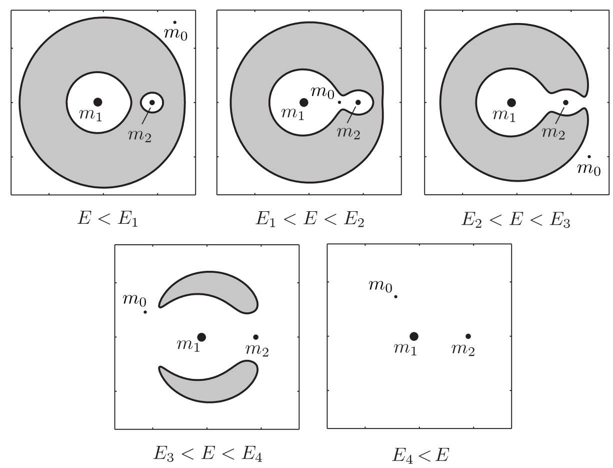

Figure 3: The Hamiltonian energy can be separated into five distinct intervals based on the topologies of the forbidden realm.

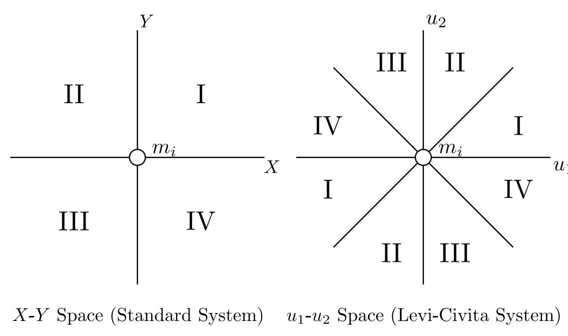

Figure 4: The x-y plane in standard coordinates maps to the half-plane in regularized coordinates.

must first resolve a methodological difficulty.

The Hamiltonian (1) diverges as $r_i \to 0$ and so the associated equations of motion are not defined at $r_i = 0$. The locations of the primaries are singularities, creating challenges for numerical and analytical investigation in arbitrarily small neighborhoods of the two masses. The

Levi-Civita regularization resolves these issues by reformulating the CR3BP in order to remove one of the singularities from the system. We assume, for the remainder of this study, that the singularity to be regularized is the singularity about m_2.

We define a Cartesian coordinate system (X, Y) centered at m_2 where $X = x - 1 + \mu$ and $Y = y$ and a corresponding polar coordinate system (r, θ) where $r = \sqrt{X^2 + Y^2}$ and $\theta = (Y, X)$.

Then, the Levi-Civita regularization recasts the phase space variables into the following form (Paez & Guzzo, 2020):

$$\begin{aligned} x - 1 + \mu &= u_1^2 - u_2^2, \\ y &= 2u_1 u_2, \\ p_x &= \frac{U_1 u_1 - U_2 u_2}{2\,|u|^2}, \\ p_y - 1 + \mu &= \frac{U_1 u_2 + U_2 u_1}{2\,|u|^2} \end{aligned} \tag{2}$$

with $|u|^2 = u_1^2 + u_2^2$ (refer to a visualization of the position space transformation in Figure 4). In addition, the standard time t is rescaled into the Levi-Civita time τ according to the conversion equation

$$dt = |u|^2\, d\tau. \tag{3}$$

Regularization recasts the singularity as a *collision manifold* (Llibre, 1982) which is included within the Levi-Civita phase space.

For topological reasons, one may extend phase space to six dimensions by including the standard time t and the standard energy E, which are conjugate to each other, so that the full set of phase space variables becomes $(u_1, u_2, U_1, U_2, t, E)$ (For notational and conceptual simplicity, t and E will be omitted in certain sections of the ensuing analysis, resulting in four-dimensional state vectors). E is constant in τ and must be set to the H_{CR3BP} energy of the trajectory under consideration.

The Hamiltonian for the Levi-Civita system is

$$\begin{aligned} H_{\mathrm{LCR}} = \frac{\left(U_1 + 2|u|^2 u_2\right)^2}{8} &+ \frac{\left(U_2 - 2|u|^2 u_1\right)^2}{8} \\ &- \frac{|u|^6}{2} - \mu - |u|^2\left(E + \frac{(1-\mu)^2}{2}\right) - \\ (1-\mu)|u|^2 &\left(\frac{1}{\sqrt{1 + 2(u_1^2 - u_2^2) + |u|^4}} + u_1^2 - u_2^2\right). \end{aligned}$$

The equations of motion corresponding to (4) are as follows:

$$\begin{aligned} \frac{du_1}{d\tau} &= \frac{\partial H_{\mathrm{LCR}}}{\partial U_1}, \\ \frac{du_2}{d\tau} &= \frac{\partial H_{\mathrm{LCR}}}{\partial U_2}, \\ \frac{dt}{d\tau} &= \frac{\partial H_{\mathrm{LCR}}}{\partial E}, \\ \frac{dU_1}{d\tau} &= -\frac{\partial H_{\mathrm{LCR}}}{\partial u_1}, \\ \frac{dU_2}{d\tau} &= -\frac{\partial H_{\mathrm{LCR}}}{\partial u_2}, \\ \frac{dE}{d\tau} &= -\frac{\partial H_{\mathrm{LCR}}}{\partial t}. \end{aligned} \tag{4}$$

Note that the third equation in (4) is equivalent to (3) and that the sixth equation in (4) implies $\frac{dE}{d\tau} = 0$.

3.4. The Levi-Civita regularization and numerical integration

Regularization facilitates numerical investigation: attempting to integrate the standard CR3BP equations of motion in the vicinity of the singularity often causes the algorithm to fail or become prohibitively slow as the step size becomes too small.

Throughout the remainder of this paper, we numerically integrate trajectories that pass near the singularity by converting standard trajectories to Levi-Civita form using the inverse forms of (2) and (3), integrating within the regularized system, and then converting back to standard coordinates.

4. Preliminary Numerical Experiments on the Stable and Unstable Manifolds to the Singularity

In this section, we demonstrate the connection between the unstable and stable manifolds to the singularity and the Arches of Chaos using several numerical experiments. All numerical experiments will occur within the context of the Sun-Jupiter PCR3BP, in which $\mu \approx 9.537 \times 10^{-4}$.

4.1. Global geometry of the stable and unstable manifolds

Generating initial conditions for trajectories along the stable and unstable manifolds to the singularity is very straightforward in standard coordinates. The stable manifold is comprised of trajectories that collide with the singularity in forward time, and the unstable manifold is comprised of trajectories that collide with the singularity in backward time. Trajectories with initial conditions $(r, \theta, -\dot{r}, 0)$ and $(r, \theta, \dot{r}, 0)$ for $0 < r \ll 1$, $\dot{r} \gg 1$, and $\theta \in S^1$ therefore shadow the stable and unstable manifolds, respectively. For fixed r and θ, an initial condition can have an $\dot{r}$ with arbitrarily large magnitude and still

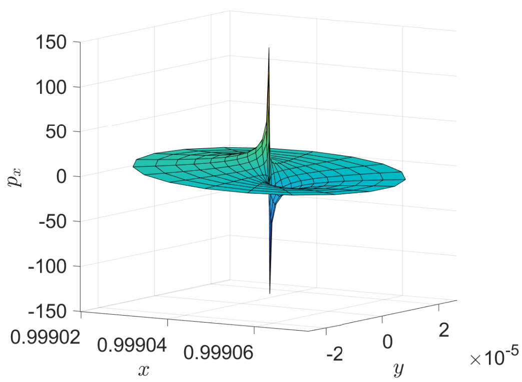

Figure 5: A projection of the portion of the stable manifold with $E = 1.3$ onto x-y-p_x space. Integration has been truncated while the trajectories are still close to the singularity in order to make the depiction of the geometry clearer.

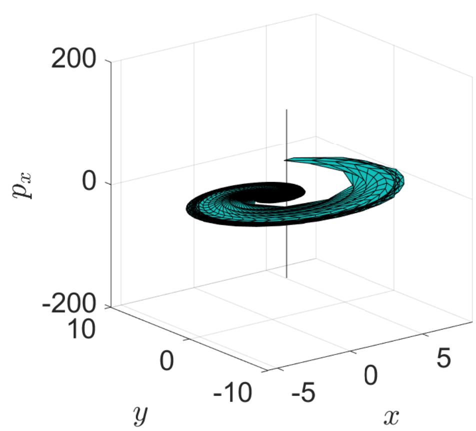

Figure 6: A projection of the portion of the stable manifold with $E = 1.3$ onto x-y-p_x space. Integration has been truncated much further from the singularity than in Figure 5.

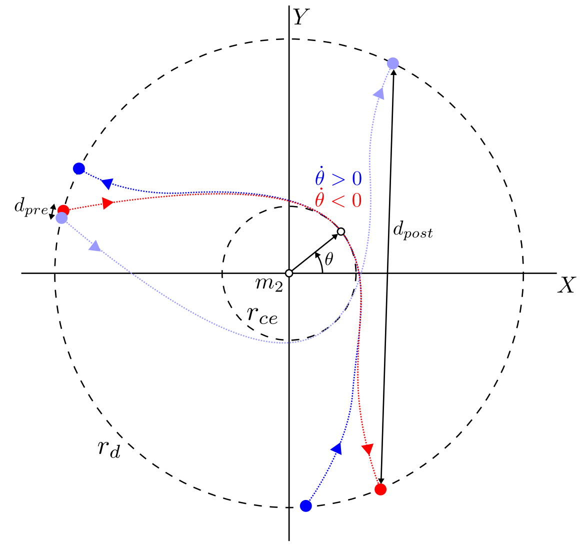

Figure 7: A schematic of the numerical experiment for examining how trajectories on either side of the stable manifold to the singularity move throughout phase space. The red and dark blue trajectories are generated at an initial radius r_{ce} but have $\dot{\theta} < 0$ and $\dot{\theta} > 0$, respectively. They reflect one choice of θ, but a whole family of trajectories for different values of θ must be generated in order to match + and - pairs along the detection radius r_d. We integrate forwards and backwards and then match those + and - trajectories whose final position in backwards time was nearest to each other; in the schematic, the red - trajectory has been matched with a light blue + trajectory, generated in the same way as the dark blue trajectory for a different value of θ. We then compare the pre-encounter, four-dimensional phase space distance d_{pre} with the post-encounter distance d_{post} for each matched pair.

lie on the manifolds, and so the stable and unstable manifolds are parameterized by the Hamiltonian energy. The stable manifold and the unstable manifold with a chosen fixed energy are diffeomorphic to $S^1 \times \mathbb{R}$ (a cylinder), and the full topology of each manifold is diffeomorphic to $S^1 \times \mathbb{R} \times \mathbb{R}$ (the Cartesian product of a cylinder and the real line).

Trajectories along the globalized stable and unstable manifolds are obtained by numerically integrating these initial conditions backwards and forwards, respectively, using the procedure described in Subsection 3.4.

The intersections of the manifolds with a fixed energy surface are straightforward to visualize. Fix $H_{CR3BP} = E$. Select a large number of linearly spaced θ, calculate the corresponding $\dot{\theta}$ at the chosen energy, and integrate. The resulting two-dimensional surface, which is embedded in the four-dimensional phase space, can be projected into three-dimensional space (see Figures 5 and 6).

4.2. Quantifying the consequences of close encounters

We demonstrate using a numerical experiment that trajectories separated by the stable and unstable manifolds to the singularity undergo phase space divergence. Without loss of generality, restrict attention to the stable manifolds of m_2 and consider the following construction:

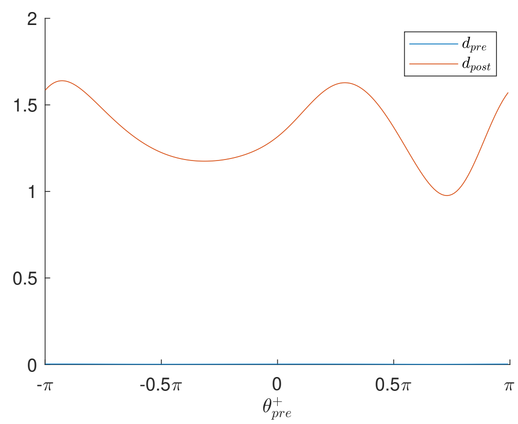

Figure 8: The + and - trajectories have an essentially constant, very small initial separation pre-encounter, but post-encounter their separation varies significantly depending on the angle along the detection circle (in this case, we use θ^+_{pre}, the pre-encounter angle of each + trajectory, as the angle for identifying and sorting matched pairs of + and - trajectories).

1. Define two circles in position space centered at m_2: a close encounter radius r_{ce} which is very small, and a detection radius r_d which is very large (at minimum, greater than the Hill radius).
2. Generate initial conditions corresponding to trajectories which have their closest approaches to the singularity at $r = r_{ce}$. As discussed in Subsection 4.1, trajectories with initial conditions $(r_{ce}, \theta, -\dot{r}, 0)$ for $\dot{r} \gg 1$ and $\theta \in S^1$ lie on the stable manifold to the singularity. The set of trajectories which have their closest encounters to the singularity at r_{ce} have perpendicular velocity vectors. This requirement translates to the initial conditions $(r_{ce}, \theta, 0, \dot{\theta}_\pm)$ for $\dot{\theta}_+ \gg 0$, $\dot{\theta}_- \ll 0$, and $\theta \in S^1$. Notice that at each fixed θ and E there are two choices of $\dot{\theta}$, which we designate $\dot{\theta}_+$ and $\dot{\theta}_-$, satisfying the construction. Distinguish close encounter trajectories of the forms $(r_{ce}, \theta, 0, \dot{\theta}_+)$ and $(r_{ce}, \theta, 0, \dot{\theta}_-)$ by the terms + *trajectories* and - *trajectories*, respectively.
3. Fix E and select a large number of linearly spaced θ, calculate their corresponding + trajectories and - trajectories, and then integrate forwards and backwards using the procedure described in Subsection 3.4 until the trajectory intersects r_d.
4. Match each - trajectory with the + trajectory whose backward-time intersection point with the r_d circle is closest to that of the - trajectory. This + trajectory will not generally be the + trajectory that was generated alongside the - trajectory under consideration. The + and - trajectories in the matched pair will encounter the singularity from different sides and therefore lie on either side of the stable manifold.
5. Once each matched pair of + and - trajectories has been determined, calculate the phase space distance d_{pre} between their backward-time intersection points with r_d and the phase space distance d_{post} between their forward-time intersection points with r_d.

Plotting d_{pre} and d_{post} as functions of the post-encounter angle of each + trajectory, we discover that although the trajectories lying on either side of the stable manifold start out extremely close together, they diverge markedly post-encounter (see 8). The extent of this divergence depends on the close encounter angle.

In addition, the two-body orbital elements of the matched pairs of + and - trajectories with respect to m_1 can be calculated for the forward-time and backward-time intersections with the detection circle. We can then plot these orbital elements, such as the Keplerian energy E and the argument of perigee ω, as a function of the pre-encounter angle of each + trajectory (see Figure 9).

4.3. Close encounters and patched conics

The close encounter behavior described in the previous subsection converges to that predicted by patched conics as $r_{ce} \to 0$ and $r_d \to 0$. As a numerical experiment to verify and explore this statement, we use the Keplerian equations with respect to m_2 to find orbital elements for the initial conditions generated according to the scheme in Figure 7. For varying choices of r_d and r_{ce}, we build initial conditions and compute the Keplerian energies and argument of perigee values at the points where each trajectory intersects the r_d circle.

Suppose r_{ce} and r_d are sufficiently small. We take $r_{ce} = \frac{R_{♃}}{180}$ and $r_d = r_h$, where r_h is the Hill radius. For these parameters, the orbital elements propagated via patched conics and the orbital elements calculated in the full three-body regime closely agree (see Figure 10).

Increase r_{ce} and fix r_d so that $r_{ce} = \frac{R_{♃}}{10}$ and $r_d = r_h$. Then we notice, by comparison with Figure 10, that the + and - trajectory values converge to the patched conics values as $r_{ce} \to 0$ (see Figure 11). The Keplerian energies and arguments of perigee of + and - trajectories generated along the detection circle at the same θ and then propagated with patched conics are in fact identical.

What if we instead increase r_d and fix r_{ce} so that $r_{ce} = \frac{R_{♃}}{180}$ and $r_d = 7r_h$? Then we notice, by comparison with Figure 10, that the patched conics curve matches phase and shape with the + and - trajectory values as $r_d \to 0$ (see Figure 12).

Computing the maximum distance between the relevant curves permits quantifying the error between the patched conics and CR3BP cases. By holding one radius constant and continuously varying the other, visualizing how the error converges to zero as the radii decrease is straightforward. Vary r_d and set $r_{ce} = \frac{R_{♃}}{180}$. We let $r_d = nr_h$, $n > 0$.

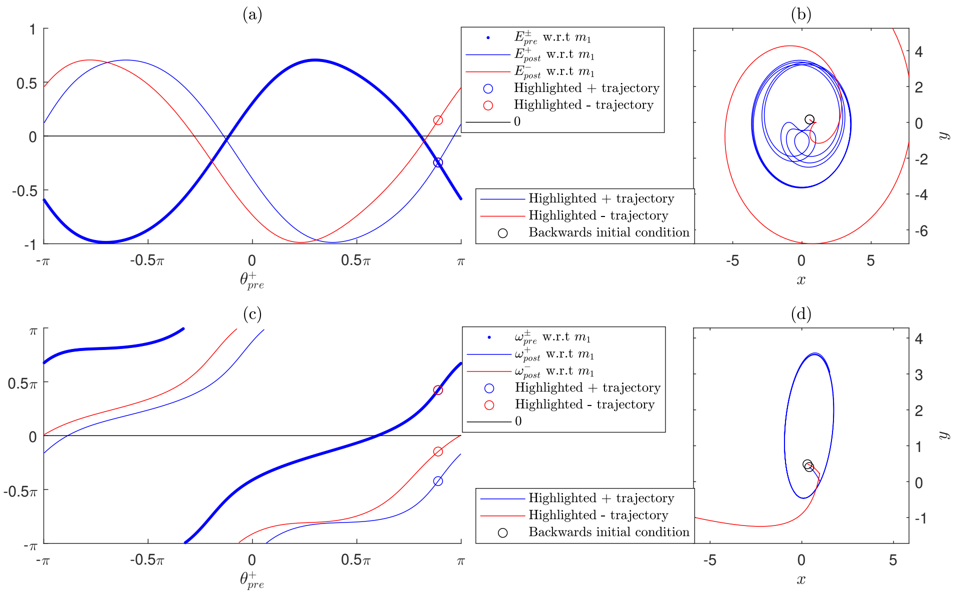

Figure 9: For all computations in this figure, trajectories were generated such that $r_d \approx 0.4774$ and $r_{ce} = 0.1R_{♃}$, where $R_{♃}$ is the radius of Jupiter in non-dimensionalized units. (a) A comparison of the Keplerian energies of the + and - trajectories as a function of the pre-encounter angle θ^{+}_{pre}. $E^{\pm}_{pre}$ denotes the pre-encounter Keplerian energies of the + and - trajectories, which approximately coincide. E^{+}_{post} and E^{-}_{post} denote the post-encounter Keplerian energies of the + and - trajectories, respectively. The energy values of an example pair of matched + and - trajectories are highlighted. The + trajectory has negative Keplerian energy after the encounter, which predicts that it will be a bound elliptical orbit around m_1; the - trajectory has positive Keplerian energy after the encounter, which predicts that it will be an unbound hyperbolic orbit. (b) The highlighted pair of + and - trajectories integrated in the rotating frame, demonstrating the predicted divergence in their post-encounter fates. (c) A comparison of the argument of periapse values of the + and - trajectories as a function of the pre-encounter angle θ^{+}_{pre}. $\omega^{\pm}_{pre}$ denotes the pre-encounter argument of perigee values of the + and - trajectories, which approximately coincide. ω^{+}_{post} and ω^{-}_{post} denote the post-encounter argument of perigee values of the + and - trajectories, respectively. The values of the example trajectories are highlighted. (d) The highlighted pair of + and - trajectories integrated in the inertial frame.

Calculating the errors in the Keplerian energy and argument of perigee over a range of n results in the behavior seen in Figure 13, in which the error decreases with n.

5. Numerically Linking the Arches of Chaos and the Stable and Unstable Manifolds

It is straightforward to demonstrate the geometric linkage between trajectories lying along the arches of chaos and the stable and unstable manifolds to the singularities. By globalizing the stable manifold to the m_2 singularity backwards until it reaches the section used to create the arches of chaos (see Subsection 2.2.1 for a specification of this section), we can determine whether the intersection of the stable manifold with this surface replicates the arch pattern in Figure 1. Previous work suggested that the connection holds in the other direction: all trajectories that have initial conditions on the section and that belong to the arch structure have close encounters with Jupiter (Todorović et al., 2020).

In order to generate initial conditions along the stable manifold, we use the approach described in Subsection 4.1 for a cylindrical grid of θ and E values. We then integrate backwards until we reach the surface of section or until the trajectory meets one of several failure criteria, namely escaping from the vicinities of m_1 and m_2, colliding with m_1, or running out of integration time.

Only a very small percentage of the trajectories forming the stable manifold reach the surface of section, but those that do reach the section form a pattern that coincides with the arches of chaos (see 14). Thus, the connection between the arches of chaos and the stable manifold to the m_2 singularity is visually apparent.

6. Discussion and Conclusion

We demonstrate, using the Levi-Civita regularization as a numerical tool, that the arches of chaos can be identified with the stable and unstable manifolds emanating from the singularities in the circular restricted three-body problem. Trajectories whose initial conditions lie near either side of the manifolds experience dramatic amounts of phase space stretching, and this implication is consistent with the construction of the original FLI plots. Plotting the orbital elements of these trajectories before and after close encounters demonstrates how the manifolds affect capture/escape behavior and how the manifolds connect to patched conics flyby theory. The numerical linkage between the arches of chaos and the stable and unstable manifolds to the singularity is uncovered by globalizing

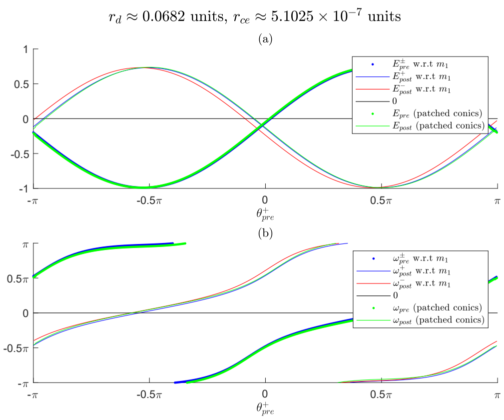

Figure 10: A comparison of selected orbital elements of the families of + and - trajectories integrated in the full PCR3BP equations with orbital elements ascertained through patched conics propagation. Both r_d and r_{ce} are small enough that close agreement is seen with the Keplerian case.

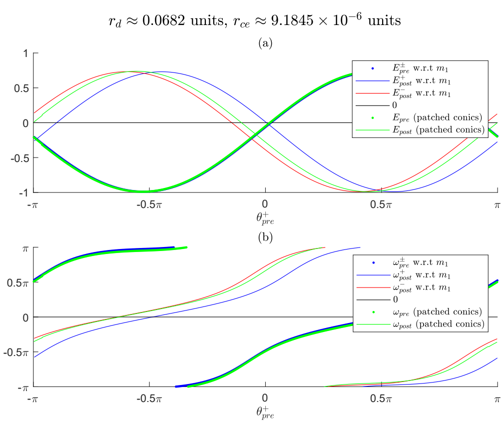

Figure 11: Similar to Figure 10, but r_{ce} has been increased.

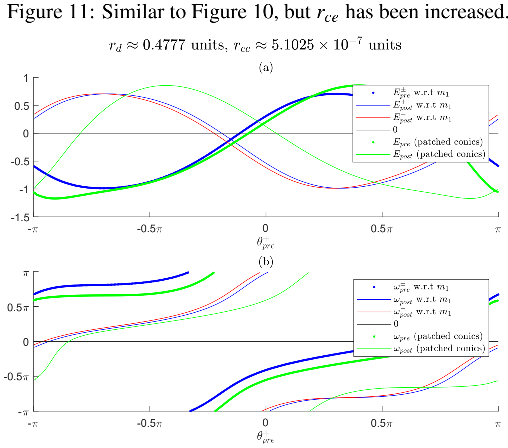

Figure 12: Similar to Figure 10, but r_d has been increased.

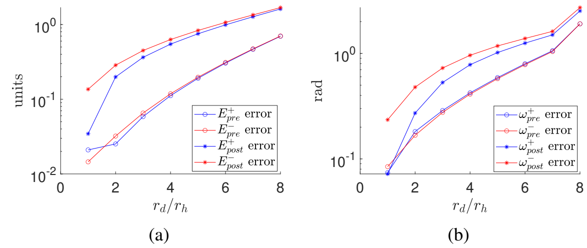

Figure 13: A comparison of the maximum errors between the three-body and patched conics orbital element curves. $n = r_d/r_h$. The error is computed with respect to the corresponding patched conics curve: for example, E_{pre} for $E^{\pm}_{pre}$ and E_{post} for $E^{\pm}_{post}$. (a) The Keplerian energy errors. (b) The argument of perigee errors.

the manifolds to the proper section.

As an explanation of the nature of the arches of chaos, we believe that our work represents a significant contribution to the literature. In addition, it unifies several related concepts: the arches, the stable and unstable manifolds to the singularities, the collision manifold, and patched conics flyby theory.

One interesting implication of our work is that the shape of the arches of chaos is not intrinsic to their function; rather, it arises from the specific choice of section with which the manifolds are intersected. The manifolds are three-dimensional objects embedded in a four-dimensional space. The choice of section used by Todorović et al. happens to depict these three-dimensional objects as a series of one-dimensional "arches" embedded in a two-dimensional orbital elements space, but the manifolds could be depicted in other ways with equal validity.

Another interesting implication of our work is that Figure 9 implies a method for designing pairs of high-energy three-body orbits whose initial conditions lie very close to each other but whose fates are very dissimilar: one will be captured by the primary and the other will escape the system. Using a Keplerian energy plot similar to the one in the figure, a θ^{+}_{pre} can be selected such that one trajectory has positive Keplerian energy with respect to the primary after encounter and the other trajectory has negative Keplerian energy with respect to the primary after encounter. This technique might facilitate the design of multi-payload missions in which the primary payload is destined for interplanetary space and the secondary payload must remain within the Earth-Moon system.

There are several potential topics for further research. Homoclinic and heteroclinic trajectories that connect Lyapunov orbits around the Lagrange points are key to understanding the global transit structure predicted by the low-energy manifold dynamics theory (Koon et al., 2022). Analyzing heteroclinic and homoclinic connections between the singularities and other dynamical objects of interest as in Paez & Guzzo (2020), particularly when perturbations capable of altering the CR3BP energy are added to the

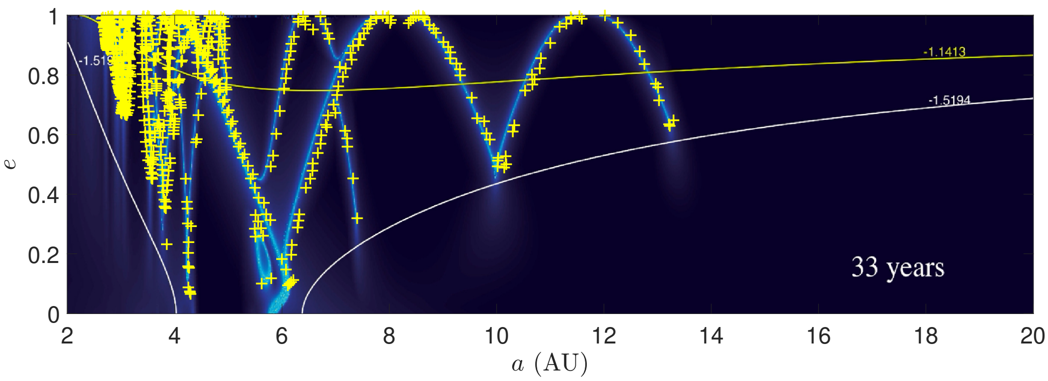

Figure 14: The intersection of an approximation of the stable manifold originally consisting of 40,000 trajectories with the arches of chaos section, viewed in semi-major axis/eccentricity space. Yellow crosses represent stable manifold trajectories, which have been superimposed onto a plot of the arches of chaos in the Sun-Jupiter-Spacecraft restricted three-body problem adapted from Todorović et al. (2020). The stable manifold closely shadows the arches even though only a small percentage of the trajectories intercept the section.

system, could facilitate the construction of an all-energy global transit structure theory. Additionally, although our work explored the arches of chaos from a purely three-body perspective, they were also introduced within a solar system model containing all major planets (Todorović et al., 2020), and recent work has confirmed using Keplerian maps that transfers between different solar system planets are possible within the low-energy regime (Werner, 2022). The possibility of constructing a theory that unifies low-energy interplanetary transfers and the full, high-energy arches of chaos should be explored further.

Acknowledgments

J.F. was supported in part by the Virginia Space Grant Consortium Graduate Research Fellowship. J.F. would like to thank Bhanu Kumar for helpful feedback during conceptual discussions.

References

Astakhov, S. A., & Farrelly, D. (2004). Capture and escape in the elliptic restricted three-body problem. *Monthly Notices of the Royal Astronomical Society*, *354*(4), 971–979.

Bartsch, T., Moix, J. M., Hernandez, R., Kawai, S., & Uzer, T. (2008). Time-dependent transition state theory. In S. A. Rice (Ed.), *Advances in Chemical Physics* (p. 191). John Wiley Sons, Inc. volume 140.

Conley, C. C. (1968). Low energy transit orbits in the restricted three-body problem. *SIAM J. Appl. Math.*, *16*, 732–746.

Conley, C. C. (1969). On the ultimate behavior of orbits with respect to an unstable critical point. I. Oscillating, asymptotic, and capture orbits. *J. Differential Equations*, *5*, 136–158.

Farquhar, R. W. (2001). The flight of ISEE-3/ICE: Origins, mission history, and a legacy. *The Journal of the Astronautical Sciences*, *49*, 23–73.

Fitzgerald, J., & Ross, S. D. (2022). Geometry of transit orbits in the periodically-perturbed restricted three-body problem. *Advances in Space Research*, .

Froeschlé, C., Gonczi, R., & Lega, E. (1997a). The fast lyapunov indicator: a simple tool to detect weak chaos. application to the structure of the main asteroidal belt. *Planetary and space science*, *45*(7), 881–886.

Froeschlé, C., Lega, E., & Gonczi, R. (1997b). Fast lyapunov indicators. application to asteroidal motion. *Celestial Mechanics and Dynamical Astronomy*, *67*(1), 41–62.

Jaffé, C., Ross, S. D., Lo, M. W., Marsden, J. E., Farrelly, D., & Uzer, T. (2002). Theory of asteroid escape rates. *Physical Review Letters*, *89*, 011101.

Jorba, A., Jorba-Cuscó, M., & Rosales, J. J. (2020). The vicinity of the Earth–Moon L_1 point in the bicircular problem. *Celestial Mechanics and Dynamical Astronomy*, *132*(2).

Koon, W. S., Lo, M. W., Marsden, J. E., & Ross, S. D. (2001). Resonance and capture of Jupiter comets. *Celestial Mechanics and Dynamical Astronomy*, *81*, 27–38.

Koon, W. S., Lo, M. W., Marsden, J. E., & Ross, S. D. (2022). Dynamical systems, the three-body problem and space mission design. In *Equadiff 99: (In 2 Volumes)* (pp. 1167–1181). World Scientific.

Kumar, B., Anderson, R. L., & de la Llave, R. (2022). Rapid and accurate methods for computing whiskered tori and their manifolds in periodically perturbed planar circular restricted 3-body problems. *Celestial Mechanics and Dynamical Astronomy*, *134*(1), 3.

Llibre, J. (1982). On the restrited three-body problem when the mass parameter is small. *Celestial mechanics*, *28*(1), 83–105.

Llibre, J., Martinez, R., & Simó, C. (1985). Transversality of the invariant manifolds associated to the Lyapunov family of periodic orbits near L2 in the restricted three-body problem. *J. Diff. Eqns.*, *58*, 104–156.

Lo, M., Williams, B. G., Bollman, W. E., Han, D., Hahn, Y., Bell, J. L., Hirst, E. A., Corwin, R. A., Hong, P. E., Howell, K. C., Barden, B., & Wilson, R. (2001). Genesis mission design. *The Journal of the Astronautical Sciences*, *49*, 169–184.

McCarthy, B. P., & Howell, K. C. (2020). Cislunar transfer design exploiting periodic and quasi-periodic orbital structures in the four-body problem. In *71st International Astronautical Congress, Virtual*.

McGehee, R. (1969). *Some homoclinic orbits for the restricted three-body problem*. Ph.D. thesis University of Wisconsin, Madison.

Onozaki, K., Yoshimura, H., & Ross, S. D. (2017). Tube dynamics and low energy Earth-Moon transfers in the 4-body system. *Advances in Space Research*, *60*(10), 2117–2132.

Oshima, K. (2022). Multiple families of synodic resonant periodic orbits in the bicircular restricted four–body problem. *Advances in Space Research*, *70*(5), 1325–1335.

Oshima, K., Topputo, F., Campagnola, S., & Yanao, T. (2017). Analysis of medium-energy transfers to the Moon. *Celestial Mechanics and Dynamical Astronomy*, *127*(3), 285–300.

Paez, R. I., & Guzzo, M. (2020). A study of temporary captures and collisions in the circular restricted three-body problem with normalizations of the levi-civita hamiltonian. *International Journal of Non-Linear Mechanics*, *120*, 103417.

Todorović, N., Wu, D., & Rosengren, A. J. (2020). The arches of chaos in the solar system. *Science Advances*, *6*(48), eabd1313.

Topputo, F. (2013). On optimal two-impulse Earth–Moon transfers in a four-body model. *Celestial Mechanics and Dynamical Astronomy*, *117*(3), 279–313.

Werner, M. A. (2022). *Multiple Gravity Assists for Low Energy Transport in the Planar Circular Restricted 3-Body Problem*. Ph.D. thesis Virginia Tech.

Wu, W., Liu, Y., Liu, L., Zhou, J., Tang, G., & Chen, Y. (2012). Pre-loi trajectory maneuvers of the chang e-2 libration point mission. *Science China Information Sciences*, *55*(6), 1249–1258.

Zhong, J., & Ross, S. D. (2021). Global invariant manifolds delineating transition and escape dynamics in dissipative systems: an application to snap-through buckling. *Nonlinear Dynamics*, *104*, 3109–3137.

Zhong, J., Virgin, L. N., & Ross, S. D. (2017). A tube dynamics perspective governing stability transitions: An example based on snap-through buckling. *International Journal of Mechanical Sciences*, . URL: `http://www.sciencedirect.com/science/article/pii/S0020740317312596`. doi:`https://doi.org/10.1016/j.ijmecsci.2017.10.040`.